Separation and Purification Technology 355 (2025) 129623

Contents lists available at ScienceDirect

Separation and Purification Technology

journal homepage: www.elsevier.com/locate/seppur

Construction of a novel MIL-100($Mn_{0.33}Er_{0.67}$) catalyst for efficient ozone removal over high humidity: unraveling the synergistic interaction between the transition metal and rare earth

Guanqing Song [a,b], Chi Song [a,b], Xiao Wang [a], Gansheng Shi [a], Guanhong Lu [a], Lu Chen [a], Jing Sun [a,b,*], Xiaofeng Xie [a,b,*]

[a] Shanghai Institute of Ceramics, Chinese Academy of Sciences, 585 Heshuo Road, Shanghai 200050, China
[b] University of Chinese Academy of Sciences, 19 (A) Yuquan Road, Beijing 100049, China

ARTICLE INFO

Editor: Jorge Bedia

Keywords:
MIL-100
Catalytic
Ozone removal
Transition metal
Rare earth

ABSTRACT

Deactivation of ozone catalysts at high humidity and their transient degradation mechanisms are two issues of interest. Herein, we constructed a group of MOFs, denoted as MIL-100(Mn), MIL-100(Er), and MIL-100 ($Mn_{0.33}Er_{0.67}$). The optimal performance was achieved by MIL-100($Mn_{0.33}Er_{0.67}$), which maintains 95% removal efficiency for more than 72 h over wide humidity fluctuation (10% RH – 90% RH). Compared to MIL-100 (Er) and MIL-100 (Mn), it has improved by 55% and 46%, respectively. Experimental and theoretical calculations indicate that the adsorption of H_2O on the above catalysts is significantly weaker than that of O_3. Distinguishing from MIL-100(Mn), the introduction of Er provided additional active sites and expedited the removal of the intermediate (O_2^-, O_2^{2-}). Unlike the shedding of an O_2 by M-O_2 to form M (M-open metal sites), the pathway by which O_3 directly attacks M-O_2 to form M-O_3 is thermodynamically spontaneous, and a new O_3 degradation mechanism was proposed.

1. Introduction

As a typical secondary atmospheric pollutant, the control of ozone has been a global challenge due to the complexity of its formation and the influence of multiple factors [1]. Ground-level ozone was previously thought to be a photochemical reaction of nitrogen oxides (NO_x) and volatile organic compounds (VOCs) under ultraviolet irradiation [2]. Although emissions of VOCs and NO_x have been effectively restrained in recent years, ozone has shown an increasing trend rather than a decline. Additionally, indoor scenes such as oceanariums, waterworks, and printing plants emit excessive ozone. Ozone pollution poses numerous knotty issues, including weather deterioration, irreversible plant damage, and threats to human health, all of which are detrimental to global ecological sustainability [3]. Against this background, combating excessive ozone is imminent for long-term development.

Catalytic technology is widely used for removing ozone because of its mild reaction conditions and high efficiency [4]. Initially, catalysts focused on transition metal oxides, such as MnO_x [5] and CoO_x [6], due to their variable valency and a profusion of oxygen vacancies. Unfortunately, these catalysts generally exhibit a rapid decay of ozone conversion rate under humid environments owing to the dominance of water in competitive adsorption with ozone [7]. Subsequently, Zhang [8] constructed water-resistant oxygen vacancies by introducing Cl into δ-MnO_2, enhancing ozone degradation performance under high humidity conditions. Guo [9] fabricated a novel dual-site catalyst, Co@Co_3O_4-C, which effectively mitigated the competitive adsorption of water by modulating electron transfer. Although these strategies have significantly improved the water resistance of transition metal oxides, their performance is often constrained by surface area and pore structure, leading to a noticeable decline in catalytic efficiency at higher space velocities [10]. (WHSV>1000 $L \cdot g^{-1} \cdot h^{-1}$).

Due to the high surface area, diverse selection of metal centers, and tunable chemical functionality, metal–organic frameworks (MOFs) exhibit significant potential in the catalytic degradation of O_3 [11]. Wang [12] found that MIL-100(Fe) performed well at high moisture (RH ≥ 40 %) but poorly in low humidity, attributing that to the involvement of H_2O in the reaction process. Inspired by this, Zang [13] designed ZZU-281, which contains coordination water and can efficiently remove O_3

* Corresponding authors at: Shanghai Institute of Ceramics, Chinese Academy of Sciences, 585 Heshuo Road, Shanghai 200050, China.
E-mail addresses: jingsun@mail.sic.ac.cn (J. Sun), xxfshcn@163.com (X. Xie).

https://doi.org/10.1016/j.seppur.2024.129623
Received 25 July 2024; Received in revised form 8 September 2024; Accepted 8 September 2024
Available online 10 September 2024

across the entire humidity range. Essentially, it is still water molecules that participate in the degradation.

In contrast to the philosophy of MOF design described above, we attempted to overcome the side effects induced by water through in situ controllable modulation. MIL-100(Mn), as a stable metal–organic framework material, has demonstrated its feasibility for ozone degradation in humid regions in our previous work [14], yet its degradation efficiency needs to be further improved. The fabrication of polymetallic sites has proven to be a promising approach, as reviewed by Karen [15]. Specifically, Li [16] found that PCN-250(Fe_2Co) has a superior performance in O_3 removal compared to PCN-250(Fe_3) with a monometallic site. Although the impact of H_2O has not been fully conquered, the feasibility of bimetallic building units has been endorsed. It is gratifying that the doping of Erbium may enhance the hydrophobicity of the catalytic agent [17]. Meanwhile, Taraneh [18] pointed out Erbium-organic framework has more reactive sites at Er(III) centers, which is advantageous for heterogeneous catalysis. The ionic radius of Er^{3+} is 88 pm, comparable to that of Mn^{2+} (80 pm), making it easier to incorporate into MIL-100(Mn) without causing significant structural distortion.

In light of the above facts, a new bimetallic MOF, MIL-100 ($Mn_{0.33}Er_{067}$), has been synthesized, achieving significant enhancement compared to MIL-100(Mn). The results of DFT reveal that the adsorption energy of H_2O at open metal sites is substantially lower than that of O_3. Crucially, the oxygen attached to the metal ($M-O_2$) is not spontaneously removed but replaced by an attack of the O_3, which provides a new perspective on the mechanism of ozone degradation.

2. Experimental

2.1. Preparation of catalysts

MIL-100($Mn_{0.33}Er_{0.67}$) was acquired by a modified solvothermal method [19], and the subscripts denote the incorporation molar ratio of elements during the synthesis process. 0.02 mol $Mn(NO_3)_2{\cdot}4H_2O$ and 0.04 mol $Er(NO_3)_3{\cdot}5H_2O$ were dissolved in ethanol, then H_3BTC was added with continuous stirring until a transparent solution was obtained. Subsequently, the attained mixture was fed into an autoclave and heated at 120 °C for 6 h. Finally, products were prepared by centrifugation and vacuum drying. (The synthesis diagram is shown in Fig. S1) A batch of samples was obtained by adjusting the proportion of precursor elements, named MIL-100(Mn) and MIL-100(Er). $Mn_{0.33}Er_{0.67}$ complex was obtained by temperature-programmed decomposition [20] as a comparative, and the detailed synthesis steps are shown in SI.

2.2. Catalyst characterization

Crystal structure information is acquired by a power X-ray diffractometer (D8 ADVANCE). The microstructure and EDS mapping of the materials were obtained through a scanning electron microscope (Hitachi SU8220). In virtue of a chemisorption analyzer (PCA-1200), O_2-TPD was obtained. TG and DSC were collected by a Thermal Analysis Mass Spectrometer (STA449C) from 30 °C to 700 °C (5 K/min). The elemental valence state and coordination environment were captured by the X-ray photoelectron spectrometer (ESCAlab250, USA). The intermediates in the ozone degradation process were monitored by in situ DRIFTS (IRTracer-100, Shimadzu).

2.3. Ozone decomposition test

Ozone removal performance was conducted with a fix-bed continuous flow reactor (i.d., = 4 mm) at ambient temperature, and the number of catalysts was 50 mg (20–40 mesh). The gas flow was 2 L/min, and the space velocity was 2400 $L{\cdot}g^{-1}{\cdot}h^{-1}$. Ozone was produced by a UV ozone generator, and the concentration of inlet O_3 was controlled at 40 ppm (±1). By adjusting the ratio of N_2 and the water bubbler, humidity can be achieved in the range of 5 %-90 %. The ozone Analyzer detected real-time ozone changes (49i, Thermo Scientific). The detailed schematic is shown in Fig. S2.

2.4. DFT calculations

Our spin-polarized density functional theory (DFT) calculations [21,22] were executed with the CP2K code [23], and the detailed information can be found in SI. For computational feasibility, the MIL-100 cluster models were constructed to investigate the adsorption behavior of O_3. As shown in Fig. 1, the MIL-100 cluster model with 124 atoms contains the Mn/Er metal node with six benzoate ligands. The Brillouin-zone integration was sampled with a Γ-centered Monkhorst-Pack mesh [24] of 2 × 2 × 1.

3. Result and discussion

3.1. Structure and textural properties of catalysts

As demonstrated in Fig. 2(a), MIL-100(Mn) showed characteristic peaks corresponding to Chen's work [25], and the typical structure of Ln-BTC [26] was found in MIL-100(Er) (Fig. S3). MIL-100($Mn_{0.33}Er_{0.67}$) exhibits peaks similar to MIL-100(Er), but with significantly lower intensity, probably due to the introduction of Mn. The morphology of MIL-100(Er) (Fig. 2(c)) and MIL-100($Mn_{0.33}Er_{0.67}$) (Fig. 2(d)) is generally consistent, indicating that the doping of Mn does not significantly affect the structure. Unexpectedly, trace amounts of spherical structures were detected in Fig. 2(d), which might be due to incomplete coordination during solvothermal leading to the formation of partial MnO [27]. As illustrated in Fig. 2(e), the elements are uniformly distributed and Mn and Er successfully integrate into the metal–organic framework. The results of ICP-OES, given in Table S1, show that the ratio of Er to Mn of MIL-100($Mn_{0.33}Er_{0.67}$) is close to the ideal structure [28], confirming the successful synthesis of this new bimetallic MOF material.

The presence of manganese and erbium was analyzed by X-ray photoelectron spectroscopy (XPS) (Fig. S4(b)). As illustrated in Fig. 3(a), the characteristic peaks of 641.4 eV and 642.8 eV are attributed to Mn^{2+} and Mn^{3+} [29], respectively. The peaks around 646 eV are satellite peaks due to the presence of Mn^{2+} [30]. Compared to MIL-100(Mn), the proportion of Mn^{2+} in MIL-100($Mn_{0.33}Er_{0.67}$) decreased from 37.8 % to 31.9 %, corresponding to the loss of electrons from Mn. In comparison to MIL-100(Er), the Er^{3+} in MIL-100($Mn_{0.33}Er_{0.67}$) shifted to a lower binding energy, from 170 eV to 169.8 eV, indicating electron gain by Er. As depicted by Fig. 3(c), C existed in the form of C-O (288.9 eV), C═O (285.3 eV), and C–C/C═C (284.7 eV) [31]. The O 1s spectrum of MIL-100($Mn_{0.33}Er_{0.67}$) is shown in Fig. 3(d), three distinct peaks are observed at 531.3 eV, 532.0 eV, and 532.9 eV, corresponding to lattice oxygen (O_{lat}), adsorbed oxygen (O_{ads}), and surface hydroxyl oxygen (O_{OH}), respectively [32]. Compared to MIL-100(Mn), the signal of O_{OH} in MIL-100($Mn_{0.33}Er_{0.67}$) shifts towards higher binding energies. This shift is attributed to the stronger coordination capability of Er^{3+}, which forms more robust coordination bonds with oxygen species, thereby enhancing the stability of hydroxyl groups [33]. The O_{ads} content of MIL-100 ($Mn_{0.33}Er_{0.67}$) (42.17 %) is higher than that in MIL-100(Mn) (40.15 %), indicating that the introduction of Er enhances the adsorbed oxygen ratio, which is beneficial for O_3 degradation. This phenomenon arises from Er substituting Mn, which modifies the charge distribution of the surrounding oxygen atoms through electron transfer [34]. The Electron density difference of MIL-100($Mn_{0.33}Er_{0.67}$) was supplemented to account for electron transfer between Mn and Er. As shown in Fig. S5, yellow indicates electron-rich regions, while blue represents electron-deficient regions. Mn sites exhibit an electron-loss trend, whereas Er sites show an electron-gain trend. The above analysis indicates electron transfer from Mn to Er in MIL-100($Mn_{0.33}Er_{0.67}$), rendering the Er sites electron-rich, which in turn facilitates the binding of electrophilic ozone.

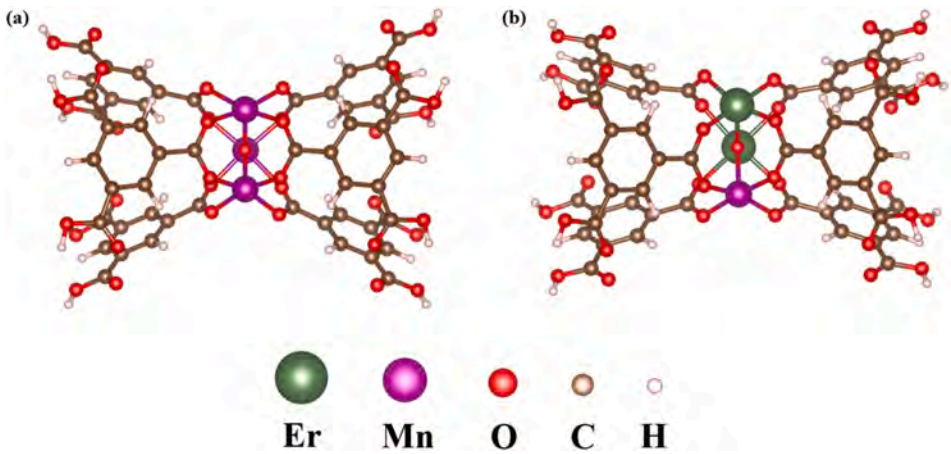

Fig. 1. The MIL-100 cluster model used for DFT calculations **(a)** MIL-100(Mn), **(b)** MIL-100($Mn_{0.33}Er_{0.67}$).

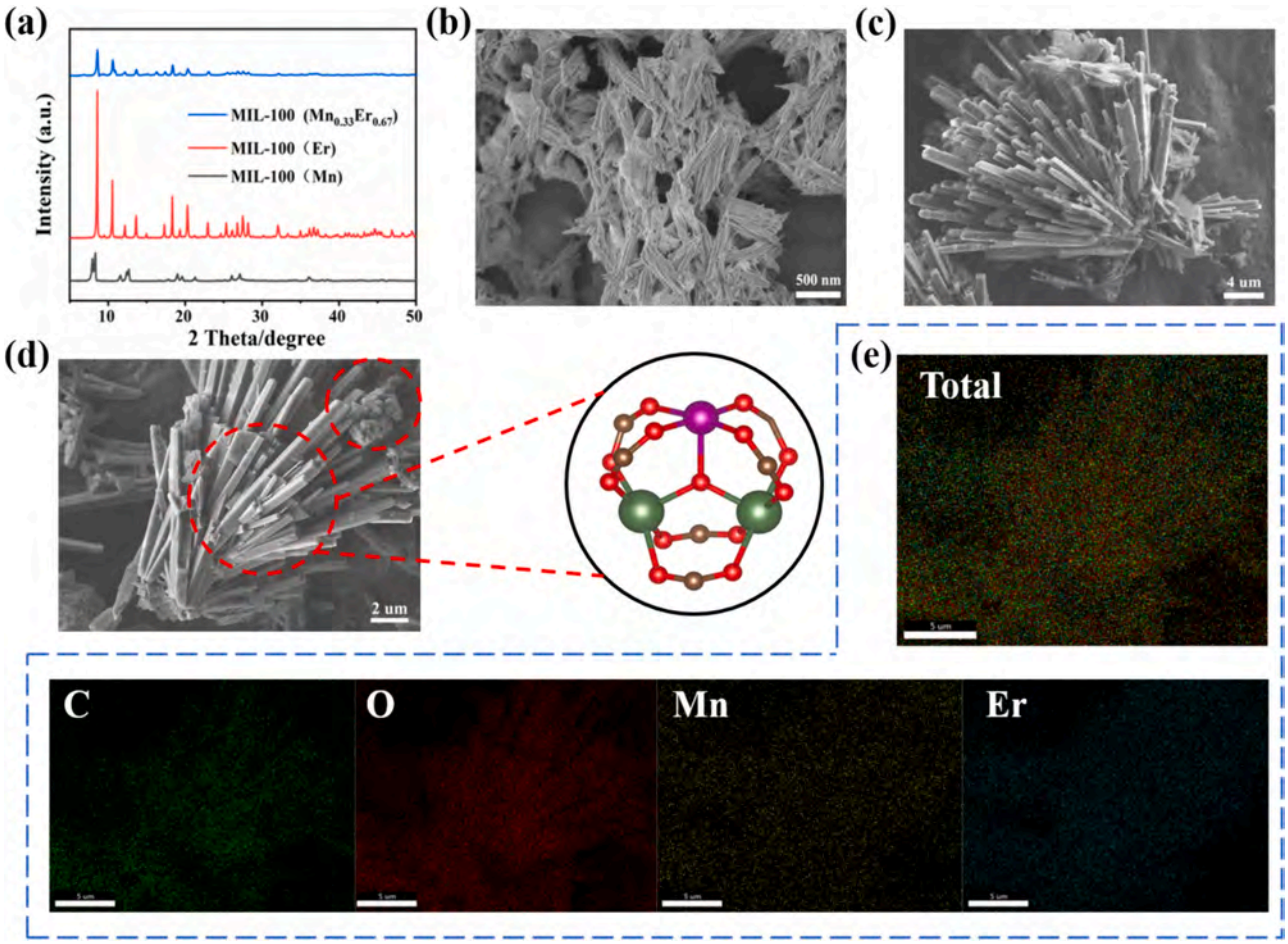

Fig. 2. **(a)** PXRD patterns of samples, SEM images of **(b)** MIL-100(Mn), **(c)** MIL-100(Er), **(d)** MIL-100($Mn_{0.33}Er_{0.67}$), **(e)** EDX elemental maps of MIL-100($Mn_{0.33}Er_{0.67}$).

3.2. Ozone degradation measurement

To approximate the actual environment, the O_3 removal test was set at 25 °C and 50 % RH. The ozone conversion efficiencies of different catalysts are shown in Fig. 4(a). MIL-100($Mn_{0.33}Er_{0.67}$) exhibited the best performance, achieving a degradation rate of 95 % over 6 h. In comparison, MIL-100(Mn) has an efficiency of 50 %, while MIL-100(Er) has only 36 %. Astonishingly, MIL-100($Mn_{0.33}Er_{0.67}$) rapidly changed color from light pink to brown within a few seconds of exposure to O_3 (Fig. S6), yet its degradation efficiency only decreased by about 5 %. Trace amounts of MnO were present during sample preparation (Fig. 2 (d)). Upon contact with O_3, MnO was converted into MnO_2. The formation of MnO_2 was believed to be responsible for the observed color change [35]. Crystal structure information before and after the reaction (Fig. S7) and the morphological changes after the reaction (Fig. S8) were provided to investigate whether MnO_2 was formed. Probably due to the

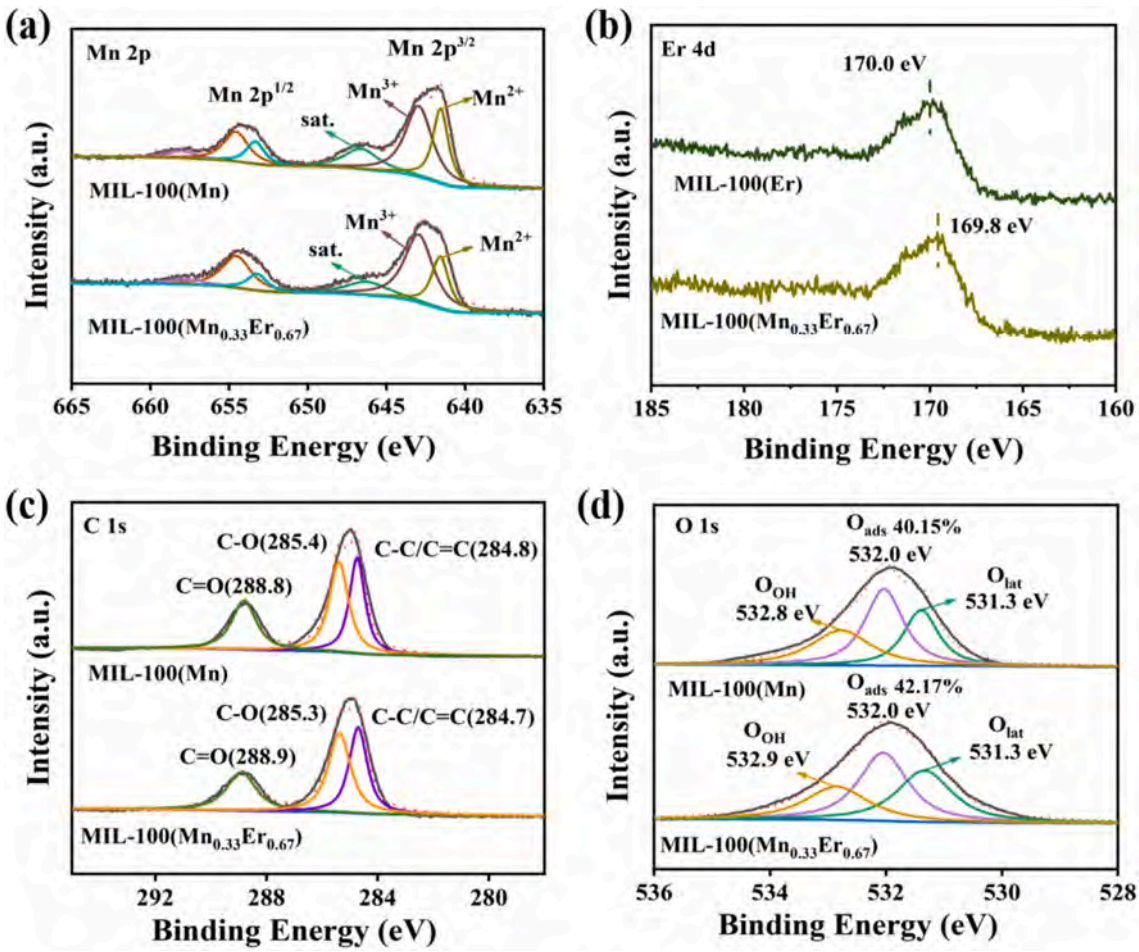

Fig. 3. The XPS of samples. **(a)** Mn 2p of MIL-100(Mn) and MIL-100($Mn_{0.33}Er_{0.67}$), **(b)** Er 4d of MIL-100(Er) and MIL-100($Mn_{0.33}Er_{0.67}$), **(c)** C 1s and **(d)** O 1s of MIL-100($Mn_{0.33}Er_{0.67}$).

low content of MnO_2, no characteristic peaks corresponding to MnO_2 were found in the XRD spectra of the reacted catalyst. A couple of spherical accumulations appeared in the morphology of the reacted samples, and Hong's research [36] identified such typical spherical cluster structures as MnO_2. XPS of MIL-100($Mn_{0.33}Er_{0.67}$) before and after the reaction was shown in Fig. S9, a small amount of Mn^{4+} (4 %) appeared in the after-reaction sample, affirming that it was the formation of MnO_2.

Water is often recognized as a major influencing factor in ozone elimination, so a large range of humidity variation was investigated (Fig. 4(b)). Ideally, the superior performance of MIL-100($Mn_{0.33}Er_{0.67}$) is virtually unaffected by moisture. According to Hong's study [37], two possible paths have been contemplated: either O_3 adsorption on MIL-100($Mn_{0.33}Er_{0.67}$) is stronger than H_2O, or water is involved in the reaction process, which we will discuss in later sections. To determine the active site for the ozone, H_3BTC, and $Mn_{0.33}Er_{0.67}$ complex were selected for comparison (Fig. 4(c)). The efficiency of the $Mn_{0.33}Er_{0.67}$ complex was about 80 %, while H_3BTC was only 10 %. Simultaneously, the adsorption process of O_3 on both the metal-oxo clusters and the organic ligands was simulated, revealing that O_3 exhibits strong interactions with the metal-oxo clusters, while its interaction with the ligands is considerably weaker. It was evident that ozone decomposition mainly occurred on the metal-oxo clusters of Mn/Er.

The stability test of the MIL-100($Mn_{0.33}Er_{0.67}$) was presented in Fig. 4(d), where we conducted a continuous 72 h test at RH-90 %. The outcome proved that MIL-100($Mn_{0.33}Er_{0.67}$) has excellent durability. O_3 concentration and space velocity are considered two critical factors influencing degradation performance. Degradation tests were conducted under varying ozone concentrations and different space velocities. The results demonstrate that under conditions of 75 ppm O_3, a space velocity of 2400 $L{\cdot}g^{-1}{\cdot}h^{-1}$, and 50 % RH, MIL-100($Mn_{0.33}Er_{0.67}$) achieved a degradation efficiency of 89 % (Fig. S10(a)). At 40 ppm O_3, with a space velocity of 1200 $L{\cdot}g^{-1}{\cdot}h^{-1}$, the degradation efficiency reached 100 % under 10 % RH and 50 % RH. (Fig. S10(b) and Fig. S10(c)). The comparison with other catalysts is listed in the table. S2, confirming the superior performance of MIL-100($Mn_{0.33}Er_{0.67}$).

Considering that ozone exists as a low-concentration mobile phase in certain scenarios, we loaded MIL-100($Mn_{0.33}Er_{0.67}$) onto ceramic honeycomb panels and integrated it into an air purification machine (Fig. S11(a)). The ozone removal test was conducted in a 20 m^3 confined space (25 °C, RH=45 %, 3800 $m^3{\cdot}h$). The highly efficient removal rate of nearly 80 % (Fig. S11(b)) demonstrates its great potential for practical application.

3.3. Exploration of degradation mechanism

The introduction of Er greatly improved the removal efficiency of O_3, which we hypothesized to be a change in the adsorption and degradation pathways of MIL-100 ($Mn_{0.33}Er_{0.67}$) [30]. Since the desorption of Oxygen-activated intermediates (O* and O_2*) is essential for ozone elimination, O_2-TPD was performed in Fig. 5(a). Contrasted with MIL-100(Mn), MIL-100($Mn_{0.33}Er_{0.67}$) showed a distinct peak at 100 °C, and the appearance of a reactive oxygen signal at lower temperatures means that intermediate removal is more likely to occur [38]. The peak observed at 208 °C, attributed to lattice oxygen [39], shifts to a higher temperature compared to that in MIL-100(Mn), indicating that the

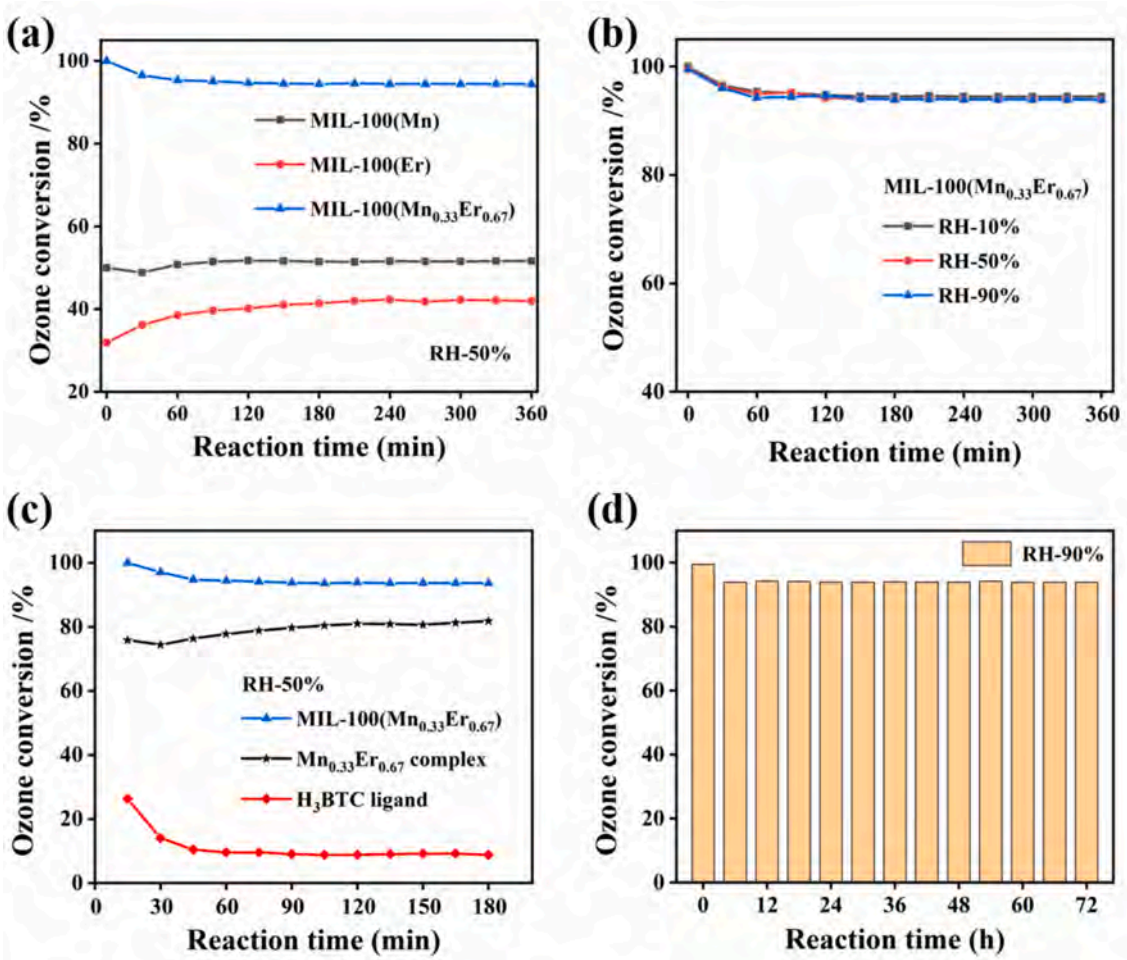

Fig. 4. The ozone conversion efficiencies of samples. **(a)** MIL-100(Mn), MIL-100(Er) and MIL-100($Mn_{0.33}Er_{0.67}$), RH-50%, **(b)** MIL-100($Mn_{0.33}Er_{0.67}$) at different humidity, **(c)** MIL-100($Mn_{0.33}Er_{0.67}$), MIL-100($Mn_{0.33}Er_{0.67}$) complex and H_3BTC, RH-50%, **(d)** Stability test of MIL-100($Mn_{0.33}Er_{0.67}$), RH-90%.

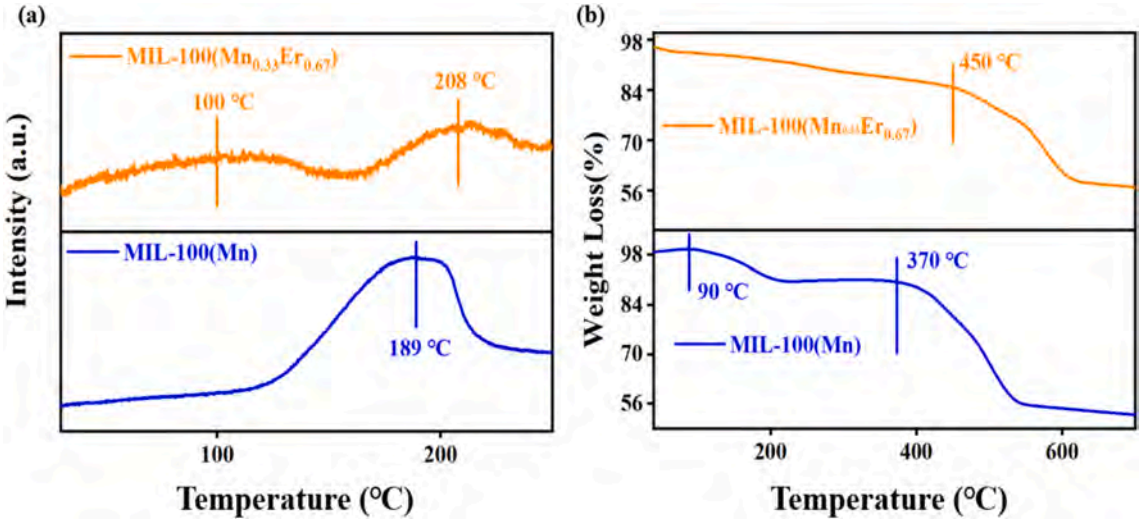

Fig. 5. **(a)** O_2-TPD, **(b)** TG of MIL-100(Mn) and MIL-100($Mn_{0.33}Er_{0.67}$).

incorporation of Er into the framework enhances the stability of MIL-100 ($Mn_{0.33}Er_{0.67}$).

Thermogravimetric tests were used to probe the thermal stability of the samples and the results are demonstrated in Fig. 5(b). The collapse of the structure of MIL-100($Mn_{0.33}Er_{0.67}$) occurred at higher temperatures compared to MIL-100(Mn), indicating that the introduction of Er is beneficial for thermodynamic stabilization. The signal at 90 °C represents the removal of adsorbed water, while the characteristic peak did not emerge on MIL-100($Mn_{0.33}Er_{0.67}$), confirming its superior water resistance.

DFT calculations were employed to simulate and analyze the adsorption and degradation pathways of ozone. Regarding adsorption, several preliminary investigations have pointed out a competitive adsorption relationship between H_2O and O_3 at open metal sites. The three possible site adsorption configurations are shown in Fig. 6, the adsorption energies of H_2O at MIL-100 (Mn)/Mn site, MIL-100 ($Mn_{0.33}Er_{0.67}$)/Mn site, and MIL-100($Mn_{0.33}Er_{0.67}$)/Er site were −0.7963 eV, −0.4282 eV, and −0.8543 eV, respectively. Remarkably, the adsorption energies of O_3 at the corresponding structures were −1.9079 eV, −1.2696 eV, and −1.6027 eV, respectively. These results manifested that O_3 is more inclined to align with MIL-100($Mn_{0.33}Er_{0.67}$) and undergo a series of reactions in this system compared to H_2O. Nevertheless, the possibility of H_2O participating in the degradation of O_3 still exists and requires further experimental evidence.

In situ infrared spectra were implemented to probe real-time changes in ozone removal, and the results are displayed in Fig. 7. The physical adsorption peak of ozone was detected at 1044 cm^{-1}, and the broadly unchanged intensity corroborated the rapidity of degradation. The signal at 2300 cm^{-1} corresponds to the adsorption of CO_2, originating from the air used to generate O_3. The peaks at 794 cm^{-1} and 950 cm^{-1} derive from the existence of O_2^- and O_2^{2-} [38], respectively, which are active oxygen groups generated during ozone decomposition. The accumulation of O_2^{2-} was essentially unchanged after 90 min, verifying the durability of the catalyst. Notably, the absence of peaks related to water in the 3000–3700 cm^{-1} range indicated that H_2O didn't participate in adsorption and subsequent degradation. These findings confirm that H_2O does not adversely affect the removal of O_3 in this system, which is consistent with the previous experimental results.

Subsequently, possible degradation pathways and corresponding active intermediates will be demonstrated individually. M-O, M-O_2, M-O_3, and M-O_4 (M-open metal sites) were detected in O_3 elimination (Fig. S12-S14). The configuration and energy of four intermediates are schematically shown in Fig. 8. Taking MIL-100($Mn_{0.33}Er_{0.67}$)/Er site as an example, the evolution of O_3 is as Fig. 8(b): The first O_3 contact with Er site and endures a strong adsorption behavior, shedding one O_2 and leaves the Er-O active group. Based on theoretical calculations, the above process is strongly spontaneous, thereby M-O is used as the initial structure for the subsequent discussions. Afterward, the second O_3 will quickly combine with the Er-O, releasing an O_2 and keeping the structure of the M-O_2. The key point is that most papers [4] have favored M-O_2 to remove an O_2 and go back to M, but this does not seem to work in our reaction system. The energy values from the fitting analysis show that the direct attack of O_3 on M-O_2 to form M-O_3 is thermodynamically spontaneous. Finally, M-O_3 releases another O_2 to form a closed loop.

The profiles of Fig. 8(a) show that each step of ozone adsorption on the Er site is an exothermic step, which is highly desirable for the

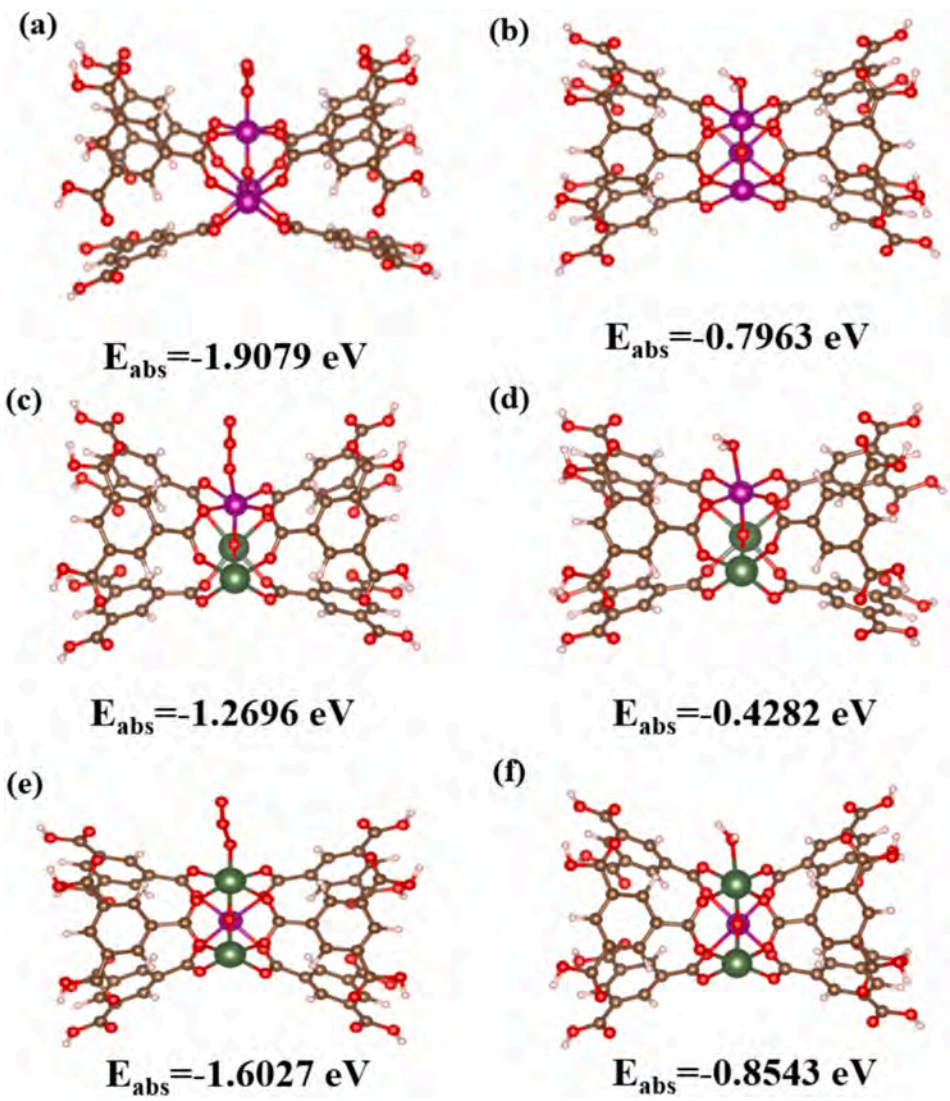

Fig. 6. Adsorption energies of O_3 and H_2O at different sites: **(a), (b)**MIL-100 (Mn)/Mn site, **(c), (d)** MIL-100($Mn_{0.33}Er_{0.67}$)/Mn site, and **(e), (f)** MIL-100 ($Mn_{0.33}Er_{0.67}$)/Er site.

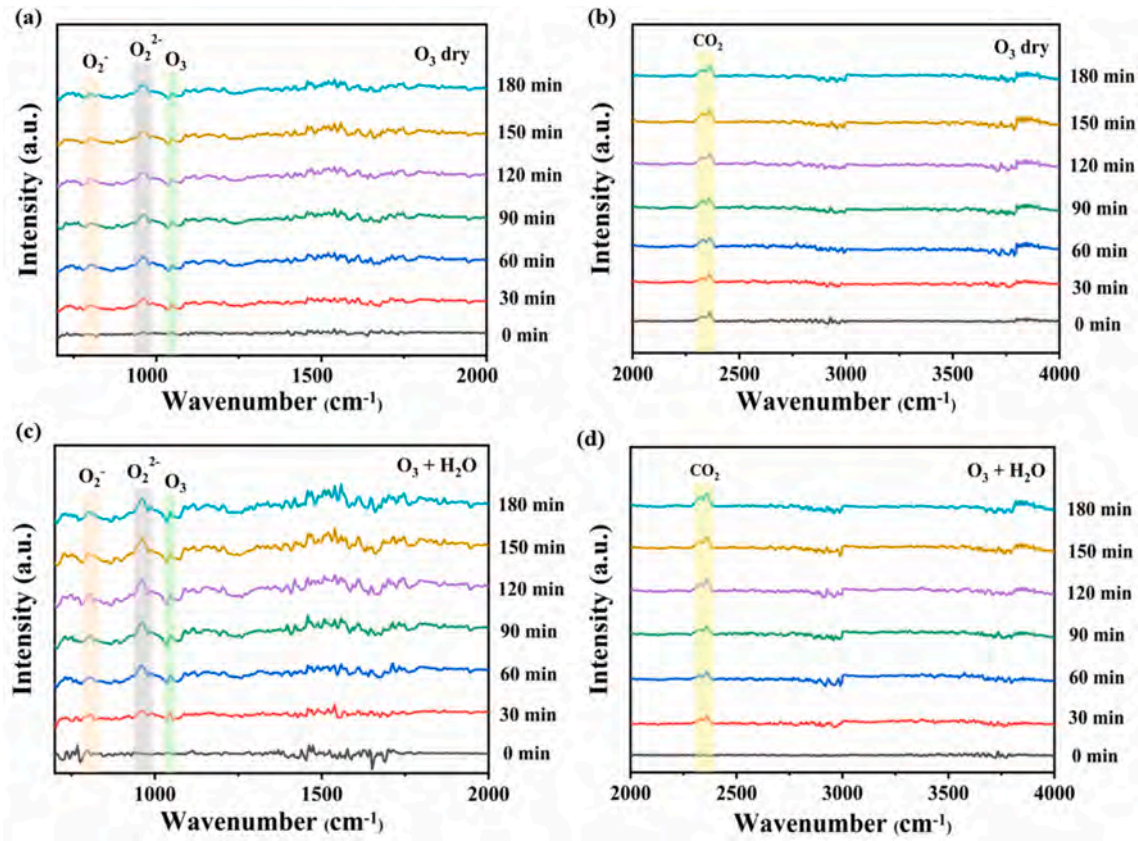

Fig. 7. In situ infrared mapping of MIL-100 ($Mn_{0.33}Er_{0.67}$) under different reaction conditions **(a), (b)** O_3 dry and **(c), (d)** $O_3 + H_2O$.

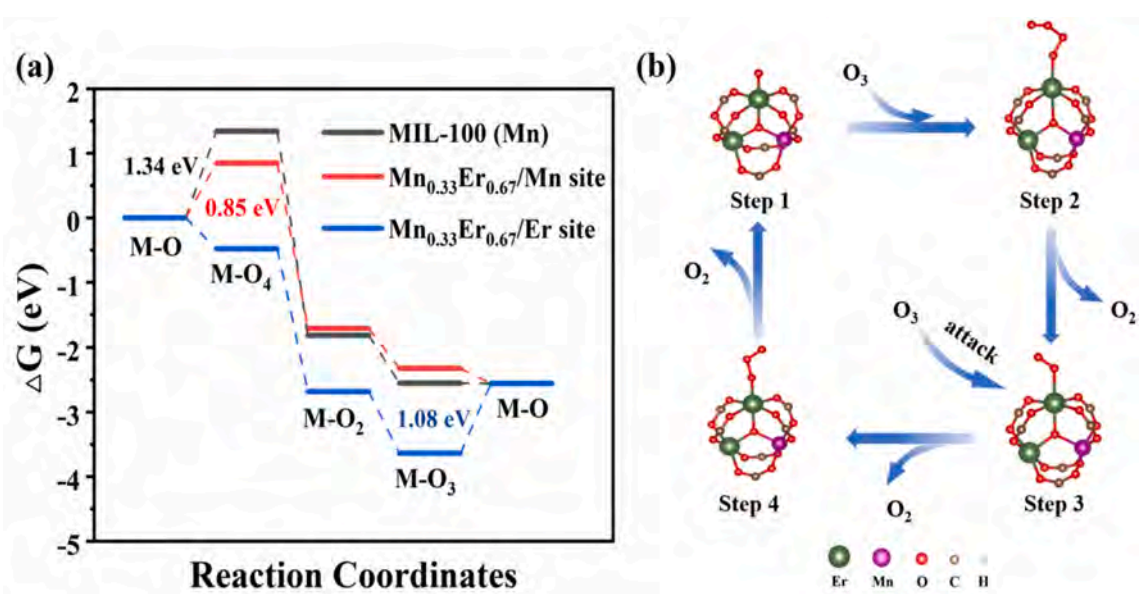

Fig. 8. Proposed reaction pathways **(a)** Reaction energy potentials at different sites, **(b)** Schema tic diagram of ozone degradation on MIL-100($Mn_{0.33}Er_{0.67}$)/Er site.

catalysis of the gas phase. Especially at lower O_3 concentrations, the overall reaction rate is more dependent on the stage of adsorbing O_3 [40]. For MIL-100(Mn), the energy required to change from M-O to M-O_4 is 1.34 eV, and the value of MIL-100($Mn_{0.33}Er_{0.67}$)/Mn site is 0.85 eV. It is obvious that the introduction of Er significantly reduces the reaction energy barrier of the Mn site, which can greatly enhance its catalytic performance.

4. Conclusion

A novel bimetallic MOF, MIL-100($Mn_{0.33}Er_{0.67}$), was successfully synthesized by the solvothermal method for ozone degradation. It nearly doubles the performance compared to MIL-100 (Mn) and maintains high efficiency over 72 h over high humidity. Differentiating from other systems, the competition of H_2O in the adsorption phase is weaker than that of O_3 and is not involved as a reactant in the subsequent proceeding.

The introduction of Er lowered the reaction barrier of the Mn site and provided a new reactive site compared to MIL-100(Mn). Remarkably, the pathway of O_3 attacking M-O_2 and releasing O_2 was verified to be more scientific in this system by experiments and DFT. The above findings provide new perspectives and thoughts on the design of materials for ozone degradation, which are expected to achieve large-scale application and industrialization of O_3 control in the future.

CRediT authorship contribution statement

Guanqing Song: Investigation, Validation, Data curation, Writing – original draft. **Chi Song:** Investigation, Methodology, Resources. **Xiao Wang:** Methodology, Formal analysis. **Gansheng Shi:** Resources. **Guanhong Lu:** Resources. **Lu Chen:** Validation. **Jing Sun:** Resources, Conceptualization, Writing – review & editing. **Xiaofeng Xie:** Conceptualization, Funding acquisition, Writing – review & editing.

Declaration of competing interest

The authors declare that they have no known competing financial interests or personal relationships that could have appeared to influence the work reported in this paper.

Data availability

Data will be made available on request.

Acknowledgment

This work was financially supported by the National Natural Science Foundation of China (52072387); Inner Mongolia Key R&D Plan (2022YFHH0049); China Postdoctoral Science Foundation (2023M740514).

Appendix A. Supplementary data

Supplementary data to this article can be found online at https://doi.org/10.1016/j.seppur.2024.129623.

References

[1] M. Evans, Ozone mystery laid to rest, Nature 570 (2019) 167–168.
[2] J. Ji, Y. Yu, S. Cao, H. Huang, Enhanced activity and water tolerance promoted by Ce on MnO/ZSM-5 for ozone decomposition, Chemosphere 280 (2021) 130664.
[3] The two faces of ozone, Nat. Clim. Change, 10 (2020) 97-97.
[4] M. Namdari, C.-S. Lee, F. Haghighat, Active ozone removal technologies for a safe indoor environment: a comprehensive review, Build. Environ. 187 (2021).
[5] G. Zhu, J. Zhu, W. Jiang, Z. Zhang, J. Wang, Y. Zhu, Q. Zhang, Surface oxygen vacancy induced α-MnO_2 nanofiber for highly efficient ozone elimination, Appl. Catal. B 209 (2017) 729–737.
[6] W.X. Tang, H.D. Liu, X.F. Wu, Y.F. Chen, Higher oxidation state responsible for ozone decomposition at room temperature over manganese and cobalt oxides: effect of calcination temperature, Ozone Sci. Eng. 36 (2014) 502–512.
[7] X. Li, J. Ma, H. He, Recent advances in catalytic decomposition of ozone, J. Environ. Sci. (China) 94 (2020) 14–31.
[8] Z. Wu, P. Zhang, S. Rong, J. Jia, Creating water-resistant oxygen vacancies in δ-MnO_2 by chlorine introduction for catalytic ozone decomposition at ambient temperature, Appl. Catal. B 335 (2023).
[9] J. Ma, W. Guo, C. Ni, X. Chen, W. Li, J. Zheng, W. Chen, Z. Luo, J. Wang, Y. Guo, Graphitized carbon-supported Co@Co(3)O(4) for ozone decomposition over the entire humidity range, Environ. Sci. Technol. 58 (2024) 12189–12200.
[10] X. Li, J. Ma, G. He, Z. Wang, H. He, In-situ formation of hydroxylated Ag active sites over Ag/MnO2 modified by alkali metals for stable decomposition of ozone under humid conditions, Appl. Catal. B: Environ. Energy 346 (2024).
[11] Y.-H. Liu, J.-A. Lv, M.-M. Xu, C. Dong, X.-M. Liu, J.-R. Li, L.-H. Xie, Birnessite-type manganese dioxide nanosheets on metal-organic frameworks with high catalytic activity in ozone decomposition, ACS Appl. Nano Mater. 6 (2023) 7794–7801.
[12] H. Wang, P. Rassu, X. Wang, H. Li, X. Wang, X. Wang, X. Feng, A. Yin, P. Li, X. Jin, S.L. Chen, X. Ma, B. Wang, An iron-containing metal-organic framework as a highly efficient catalyst for ozone decomposition, Angew. Chem. Int. Ed. Engl. 57 (2018) 16416–16420.
[13] Z.B. Sun, Y.N. Si, S.N. Zhao, Q.Y. Wang, S.Q. Zang, Ozone decomposition by a manganese-organic framework over the entire humidity range, J. Am. Chem. Soc. 143 (2021) 5150–5157.
[14] G. Song, G. Shi, L. Chen, X. Wang, J. Sun, L. Yu, X. Xie, Different degradation mechanisms of low-concentration ozone for MIL-100(Fe) and MIL-100(Mn) over wide humidity fluctuation, Chemosphere 308 (2022).
[15] S. Abednatanzi, P. Gohari Derakhshandeh, H. Depauw, F.X. Coudert, H. Vrielinck, P. Van Der Voort, K. Leus, Mixed-metal metal-organic frameworks, Chem. Soc. Rev. 48 (2019) 2535–2565.
[16] C. Dong, J.J. Yang, L.H. Xie, G. Cui, W.H. Fang, J.R. Li, Catalytic ozone decomposition and adsorptive VOCs removal in bimetallic metal-organic frameworks, Nat. Commun. 13 (2022) 4991.
[17] I.-K. Oh, K. Kim, Z. Lee, K.Y. Ko, C.-W. Lee, S.J. Lee, J.M. Myung, C. Lansalot-Matras, W. Noh, C. Dussarrat, H. Kim, H.-B.-R. Lee, Hydrophobicity of rare earth oxides grown by atomic layer deposition, Chem. Mater. 27 (2014) 148–156.
[18] T. Hajiashrafi, M. Karimi, A. Heydari, A.A. Tehrani, Erbium-organic framework as heterogeneous lewis acid catalysis for hantzsch coupling and tetrahydro-4H-chromene synthesis, Catal. Lett. 147 (2016) 453–462.
[19] Y. Ha, M. Mu, Q. Liu, N. Ji, C. Song, D. Ma, Mn-MIL-100 heterogeneous catalyst for the selective oxidative cleavage of alkenes to aldehydes, Catal. Commun. 103 (2018) 51–55.
[20] H. Huang, S. Zhou, C. Yu, H. Huang, J. Zhao, L. Dai, J. Qiu, Rapid and energy-efficient microwave pyrolysis for high-yield production of highly-active bifunctional electrocatalysts for water splitting, Energ. Environ. Sci. 13 (2020) 545–553.
[21] P. Hohenberg, W. Kohn, Inhomogeneous electron gas, Phys. Rev. 136 (1964) B864–B871.
[22] W. Kohn, L.J. Sham, Self-consistent equations including exchange and correlation effects, Phys. Rev. 140 (1965) A1133–A1138.
[23] J. VandeVondele, M. Krack, F. Mohamed, M. Parrinello, T. Chassaing, J. Hutter, Quickstep: fast and accurate density functional calculations using a mixed Gaussian and plane waves approach, Comput. Phys. Commun. 167 (2005) 103–128.
[24] H.J. Monkhorst, J.D. Pack, Special points for Brillouin-zone integrations, Phys. Rev. B 13 (1976) 5188–5192.
[25] D. Chen, Y. Zhang, P. Mao, X. Jiang, J. Li, A. Sun, J. Shen, Carbon black supported on a Mn-MIL-100 framework as high-efficiency electrocatalysts for nitrophenol reduction, J. Electroanal. Chem. 903 (2021).
[26] J. Luo, H. Xu, Y. Liu, Y. Zhao, L.L. Daemen, C. Brown, T.V. Timofeeva, S. Ma, H. C. Zhou, Hydrogen adsorption in a highly stable porous rare-earth metal-organic framework: sorption properties and neutron diffraction studies, J. Am. Chem. Soc. 130 (2008) 9626–9627.
[27] L. Chen, X. Wang, Z. Rao, Z. Tang, Y. Wang, G. Shi, G. Lu, X. Xie, D. Chen, J. Sun, In-situ synthesis of Z-Scheme MIL-100(Fe)/α-Fe2O3 heterojunction for enhanced adsorption and Visible-light photocatalytic oxidation of O-xylene, Chem. Eng. J. 416 (2021).
[28] Y. Wang, H. Lv, E.S. Grape, C.A. Gaggioli, A. Tayal, A. Dharanipragada, T. Willhammar, A.K. Inge, X. Zou, B. Liu, Z. Huang, A tunable multivariate metal-organic framework as a platform for designing photocatalysts, J. Am. Chem. Soc. 143 (2021) 6333–6338.
[29] L. Zhang, J. Yang, A. Wang, S. Chai, J. Guan, L. Nie, G. Fan, N. Han, Y. Chen, High performance ozone decomposition spinel (Mn, Co)$_3O_4$ catalyst accelerating the rate-determining step, Appl. Catal. B 303 (2022).
[30] W. Li, X. Guo, P. Geng, M. Du, Q. Jing, X. Chen, G. Zhang, H. Li, Q. Xu, P. Braunstein, H. Pang, Rational design and general synthesis of multimetallic metal-organic framework nano-octahedra for enhanced Li–S battery, Adv. Mater. 33 (2021).
[31] Z. Xie, Z. Lyu, J. Wang, A. Li, P. François-Xavier Corvini, Ultrafine-Mn2O3@N-doped porous carbon hybrids derived from Mn-MOFs: dual-reaction centre catalyst with singlet oxygen-dominant oxidation process, Chem. Eng. J. 429 (2022).
[32] G. Song, C. Shen, D. Bassir, Q. Li, A symmetry concept for the self-assembly synthesis of Mn-MIL-100 using a capping agent and its adsorption performance with methylene blue, Symmetry 15 (2023).
[33] X. Wang, D. Du, H. Xu, Y. Yan, X. Wen, L. Ren, C. Shu, NiMn-based metal-organic framework with optimized eg orbital occupancy as efficient bifunctional electrocatalyst for lithium-oxygen batteries, Chem. Eng. J. 452 (2023).
[34] W. Zhang, K. Xie, Y.H. Tang, C. Qin, S. Cheng, Y. Ma, Application of transition metal based MOF materials in selective catalytic reduction of nitrogen oxides br, Prog. Chem. 34 (2022) 2638–2650.
[35] C. Dong, T. He, W. Wu, G.-R. Si, L.-H. Xie, J.-R. Li, Visible ozone detection and removal in two-dimensional Mn(ii)-based metal–organic frameworks, J. Mater. Chem. A (2024).
[36] W. Hong, M. Shao, T. Zhu, H. Wang, Y. Sun, F. Shen, X. Li, To promote ozone catalytic decomposition by fabricating manganese vacancies in ε-MnO2 catalyst via selective dissolution of Mn-Li precursors, Appl. Catal. B 274 (2020).
[37] W. Hong, J. Ma, T. Zhu, H. He, H. Wang, Y. Sun, F. Shen, X. Li, To enhance water resistance for catalytic ozone decomposition by fabricating H_2O adsorption-site in OMS-2 tunnels, Appl. Catal. B 297 (2021).
[38] Y. Yu, H. Wang, H. Li, P. Tao, T. Sun, Influence of water molecule on active sites of manganese oxide-based catalysts for ozone decomposition, Chemosphere 298 (2022) 134187.
[39] B. Zhang, J. Ji, B. Liu, D. Zhang, S. Liu, H. Huang, Highly efficient ozone decomposition against harsh environments over long-term stable amorphous MnOx catalysts, Appl. Catal. B 315 (2022).
[40] F.J. Beltrán, J. Rivas, P. Álvarez, R. Montero-de-Espinosa, Kinetics of heterogeneous catalytic ozone decomposition in water on an activated carbon, Ozone: Sci. Eng. 24 (2007) 227–237.